International Journal of Bioprinting

RESEARCH ARTICLE

Silk fibroin–gelatin photo-crosslinked 3D-bioprinted hydrogel with MOF-methylene blue nanoparticles for infected wound healing

Zhuoyuan Li[1†], Ao Zheng[2,3†], Zhiyuan Mao[1], Fupeng Li[4], Tingshu Su[2,3], Lingyan Cao[2,3], Wei Wang[5*], Yang Liu[6*], Chen Wang[1*]

[1]Department of Plastic and Reconstructive Surgery, Shanghai Ninth People's Hospital, Shanghai Jiao Tong University School of Medicine, Shanghai, 200011, China

[2]Department of Prosthodontics, Shanghai Ninth People's Hospital, Shanghai Jiao Tong University School of Medicine; College of Stomatology, Shanghai Jiao Tong University, Shanghai, 200011, China

[3]National Center for Stomatology; National Clinical Research Center for Oral Diseases; Shanghai Key Laboratory of Stomatology; Shanghai Engineering Research Center of Advanced Dental Technology and Materials, Shanghai, 200011, China

[4]Shanghai Ninth People's Hospital, Shanghai Jiao Tong University School of Medicine, Shanghai, 200011, China

[5]Department of Orthopedic Surgery, Shanghai Sixth People's Hospital Affiliated to Shanghai Jiao Tong University School of Medicine, Shanghai, 200233, China

[6]Department of Otolaryngology, Eye & ENT Hospital, Fudan University, Shanghai, 200031, China

Abstract

Photo-crosslinked hydrogel (PH) is an outstanding candidate for three-dimensional (3D) printing as a wound dressing because of its high efficiency in crosslinking and injectability. In this study, methylene blue (MB)-loaded UiO-66(Ce) nanoparticles (NPs) were synthesized to prevent drug self-aggregation and achieve the photodynamic therapy (PDT) effect for efficient antibacterial action. Then, a composite photo-crosslinked silk fibroin (SF)/gelatin hydrogel loaded with MB@UiO-66(Ce) NPs (MB@UiO-66(Ce)/PH) was fabricated. The printability and the improvement of the mechanical properties of the hydrogel by the NPs were clarified. The hydrogel exhibited good biocompatibility and promoted the migration and proliferation of fibroblasts. With the PDT effect of MB@UiO-66(Ce) NPs, the hydrogel showed an excellent antibacterial effect, which became more pronounced as the concentration increased. *In vivo* study showed that the MB@UiO-66(Ce)/PH could fill the defects without gaps and accelerate the repair rate of full-thickness skin defects in mice. The MB@UiO-66(Ce)/PH with antibacterial properties and tissue healing-promoting ability provides a new strategy involving 3D bioprinting for preparing wound dressings.

Keywords: 3D bioprinting; Nanoparticles; Silk fibroin; Antibacterial; Photodynamic therapy; Wound healing

---

[†]These authors contributed equally to this work.

***Corresponding authors:**
Chen Wang
(wangchen2369@163.com)

Yang Liu
(ly1989rz@126.com)

Wei Wang
(xiaowangwei_ok@126.com)

Citation: Li Z, Zheng A, Mao Z, *et al*., 2023, Silk fibroin–gelatin photo-crosslinked 3D-bioprinted hydrogel with MOF-methylene blue nanoparticles for infected wound healing. *Int J Bioprint,* 9(5): 773. https://doi.org/10.18063/ijb.773

Received: February 10, 2023
Accepted: May 01, 2023
Published Online: June 13, 2023

1. Introduction

Skin is the largest organ of the human body and is vulnerable to various types of traumas, such as wounds. Wound healing has been an ongoing topic of research and an area of concern in the medical field[1]. When skin trauma occurs, the skin's protective barrier is damaged, leaving the wound site vulnerable to invasion by microorganisms in the environment, which can lead to severe infection[2]. Moreover, bacteria-associated wound infection prevents wound healing and may be life-threatening[3,4]. Therefore, wound management in the early stages is essential for preventing wound infection and promoting wound healing. Currently, wound dressings that contain antiseptics or antibiotics are commonly used to prevent and treat wound infections. However, these dressings have significant limitations, including long-term treatment, inefficacy, and high cost[5-7]. Long-term use of antibiotics can lead to bacterial resistance, which is a major clinical problem[8,9]. Therefore, it is necessary to develop a new type of non-antibiotic multifunctional wound dressing with antibacterial properties that can reduce the risk of wound infection caused by bacteria and promote wound healing.

Hydrogels have been widely used in skin, fat, and vessel tissue engineering due to their advantages including good hydrophilicity and biocompatibility[10]. Hydrogels have a similar 3D porous structure to the extracellular matrix, making them one of the most competitive candidates for wound dressings[11-13]. Meanwhile, hydrogels can maintain the high moisture level of the wound bed; therefore, hydrogels can provide an optimal 3D environment for cells to promote soft tissue regeneration[14]. Furthermore, hydrogels can be a platform for loading cells, antimicrobial agents, growth factors, and unique complementary and biological macromolecules[15].

3D bioprinting is a promising technology in the manufacture of hydrogels, offering a high degree of flexibility and reproducibility. The three most commonly used bioprinting techniques according to the American Society for Testing and Materials are jetting-based, extrusion-based, and vat photopolymerization-based bioprinting processes. The inkjet technique offers the advantages of low cost and fast printing speed but has the limitations of low accuracy and need for low-viscosity bioinks[16]. The vat photopolymerization technique offers higher resolution and accuracy than other bioprinting techniques. The high-resolution printing facilitates the fabrication of bionic mircoorganisms. However, its complex design, limited choice of biocompatible materials, and cumbersome operation hinder its wide application in the field of tissue engineering[17]. Extrusion bioprinting is the most common bioprinting technology available today. It has the advantage of simplicity of operation, but cell viability is reduced[18]. For this experiment, extrusion-based bioprinting was chosen because the hydrogel dressings are cell-free, and the structure does not require high-resolution printing. Hydrogels can be deposited layer by layer to fabricate artificial skin tissue with porous structures customized through computer-aided design[19,20]. Moreover, various photo-crosslinked polymers have been widely incorporated as a material for 3D-bioprinted tissue-engineered scaffolds due to their mild reaction conditions, highly tunable mechanical and structural properties, printability, biodegradability, and biocompatibility[19,21]. Natural polymers, which can be used as biological inks, such as alginate, gelatin, and SF, have recently attracted wide attention[22-26].

Silk fibroin (SF) extracted from *Bombyx mori*, which has good biocompatibility, adjustable biodegradability, and mechanical properties, has been used in various biomedical applications and was approved by the U.S. Food and Drug Administration (FDA) for use in drug delivery and surgical suture applications[27,28]. SF can be prepared into scaffolds, films, hydrogels, *etc.*, to meet different clinical needs. It was reported that ultrasound or chemical crosslinkers could induce the formation of SF hydrogels[29]. However, the addition of ultrasound or toxic chemical crosslinkers is not conducive to the clinical promotion of SF hydrogels. Photo-crosslinking technology can be used to prepare SF hydrogels in a controllable manner without chemical grafting or the introduction of toxic chemical crosslinking agents[30]. Previous studies have shown that by using riboflavin (RPS) and sodium persulfate (SPS) as a photoinitiator under blue light irradiation, the tyrosine (Tyr) on the molecular chain of SF can be combined to form a stable tyrosine–tyrosine (Tyr–Tyr) bond[30].

Moreover, the SF hydrogel may have difficulty meeting the needs of tissue regeneration due to its relatively dense internal pores and slow degradation[29]. The β-sheet formation in SF hydrogels could cause changes to the internal structure, compressing the internal pores and water content. Therefore, it is necessary to introduce other components to control the conformational changes of SF. The introduction of other polymers can reduce the contact between SF molecules, thereby preventing the formation of the β-sheet as well as regulating the mechanical properties for soft tissue engineering[31]. Gelatin, a natural polymer with high biocompatibility and a cell attachment sequence that is similar to the extracellular matrix, has excellent performance in cell fixation and proliferation[32]. It contains about 1% of Tyr residues in the amino acid sequence of the gelatin strands, which can be crosslinked with the SF molecular chain through Tyr–Tyr bonding without chemical modifications. Adding gelatin as a spacer molecule to the

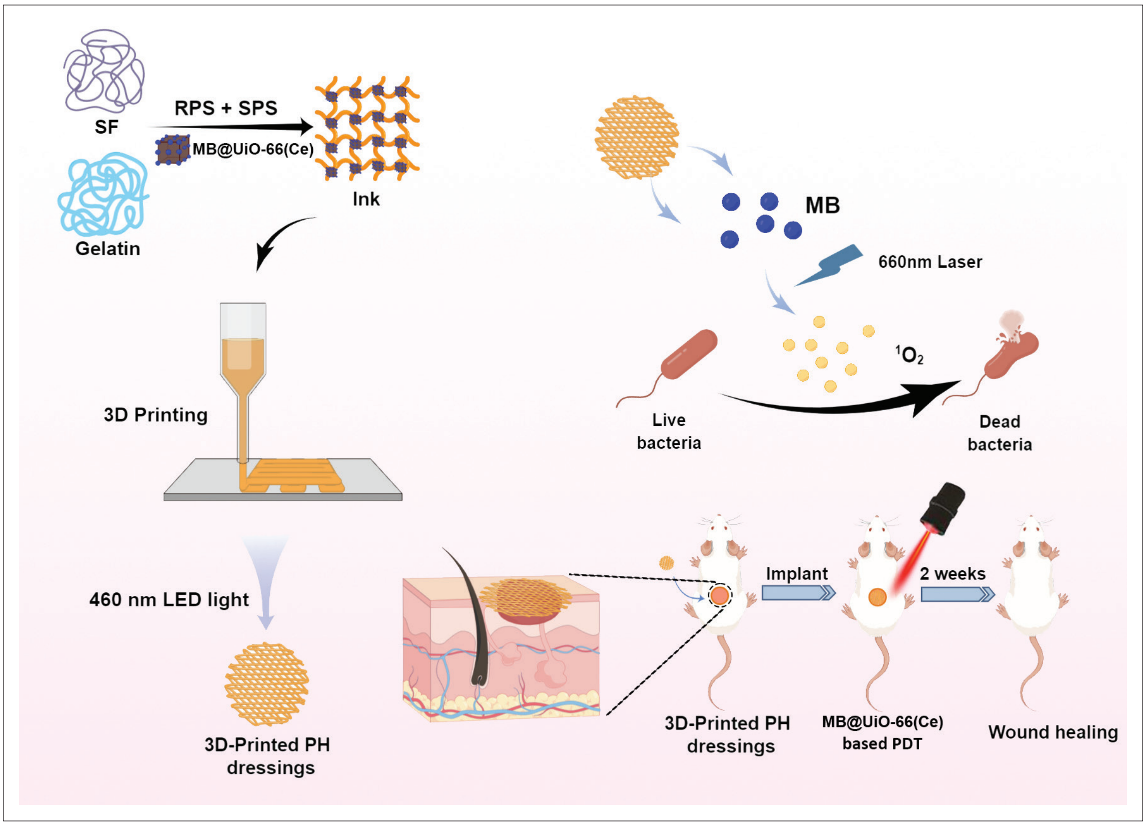

Figure 1. Schematic representation for the design strategy and applications of composite SF/gelatin 3D-bioprinted photo-crosslinked hydrogel for repairing full-thickness skin wound. Diagram created with Figdraw.

SF solution offers the advantages of improving internal structures, adjusting mechanical properties, and enhancing cell adhesion in composite hydrogels. The conformational change in SF can be avoided by adding gelatin. At the same time, tyramine in gelatin can participate in a reaction in RPS and SPS photo-crosslinking systems to form a stable, double-network hydrogel.

To avoid related clinical problems caused by antibiotic abuse, researchers are actively exploring alternative therapies, including photodynamic therapy (PDT). As an alternative strategy, PDT has attracted widespread attention for the treatment of bacterial infections[33]. The antibacterial principle of PDT is that the photosensitizer, including methylene blue (MB), toluidine blue, and texaphyrins, produces single-line oxygen ($^1O_2$) with bacterial toxicity under the action of a specific wavelength of light[34]. The MB-derived chemical is a commonly used photosensitizer and near-infrared dye that has been approved for clinic application in PDT[35,36]. Because nanoparticles (NPs) are excellent drug carriers, they are actively used in the research and application of PDT. A metal–organic framework (MOF) is an organic–inorganic hybrid material with intramolecular pores formed by the self-assembly of organic ligands and metal ions through coordination bonds. With the advantages of easy synthesis and high durability, MOFs are widely used in biomedical research[37,38]. Due to their large specific surface area and high and continuous porosity, MOFs offer advantages as a drug delivery system, including high drug load ability and controllable release[39-41]. UiO-66(Ce) is a newly developed MOF that has been widely used with good stability in the study of drug delivery systems[42]. Studies have shown that employing UiO-66 as the photosensitizer carrier in PDT achieves high drug loading and antibacterial action[43].

In this study, MB was loaded onto UiO-66(Ce) to construct MB@UiO-66(Ce) NPs. A new cell-free 3D-bioprinted dressing was prepared using photo-crosslinked hydrogels consisting of SF/gelatin composite NPs crosslinked with the MB@UiO-66(Ce) in the RPS and SPS composite. A Cell Counting Kit 8 (CCK-8) assay and a live/dead assay were used to detect the biocompatibility of the dressings. In addition, the antimicrobial effect of the hydrogel dressing against *Staphylococcus aureus* and *Escherichia coli* was evaluated, and the wound healing effect was evaluated using a mouse model of *S. aureus* infection with total skin defects (Figure 1). In general, a new cell-free

Table 1. Parameter of MB@UiO-66(Ce)/PH samples

Sample name	SF (mg/mL)	Gelatin (mg/mL)	RPS (mg/mL)	SPS (mg/mL)	MB@UiO-66(Ce) (mg/mL)
PH-0	30	50	0.013	2.382	0
PH-0.1	30	50	0.013	2.382	0.01
PH-0.5	30	50	0.013	2.382	0.05
PH-1	30	50	0.013	2.382	0.1

Abbreviations: SF, silk fibroin; RPS, riboflavin; SPS, sodium persulfate.

MB@UiO-66(Ce) composite SF/gelatin 3D-bioprinted photo-crosslinked hydrogel system was developed to promote soft tissue regeneration in the infected area.

2. Materials and methods

2.1. Materials

Bombyx mori cocoons were purchased from Jiangsu Province, China. Type A gelatin, riboflavin (5'-phosphate sodium salt hydrate), and sodium persulfate were purchased from Sigma-Aldrich, USA. LIVE/DEAD kits were ordered from YESAN, China. Dulbecco's Modified Eagle Medium (DMEM) and 100 U/mL penicillin and streptomycin were ordered from HyClone, USA. Fetal bovine serum (FBS) was ordered from Gibco, USA. FITC-phalloidin and DAPI were obtained from Invitrogen, USA. CCK-8 assay kits were purchased from Beyotime, China.

2.2. Preparation of silk fibroin

SF was extracted from *Bombyx mori* cocoons according to the following protocol[29]. First, domestic silk moths were subjected to boiling in a 0.5 wt% Na_2CO_3 solution for 30 min, which was repeated three times, and then dried in an oven at 60°C. A ternary solution was prepared with the molar ratio of $CaCl_2$: water: ethanol = 1:8:2. The dried, degummed silk cocoons were then dissolved in the ternary solution, followed by dialysis in deionized water for 3 days (MW = 3500). Finally, the SF was obtained by freeze-drying.

2.3. Synthesis of nanoscale MB@UiO-66(Ce)

First, the F127@UiO-66(Ce) samples were synthesized. Briefly, F127 (112.5 mg) was dissolved in 27 mL deionized water. Then, 2250 mg $NaClO_4$ H_2O, 0.3375 mL acetic acid, and 0.675 mL HNO_3 were added and stirred to form a homogeneous mixture. Then, 616.5 mg $(NH_4)_2Ce(NO_3)_6$ and 186.75 mg benzenedicarboxylic acid (BDC) were added to the mixture, followed by stirring for 20 min at 60°C. After that, the F127@UiO-66(Ce) particles were suspended in a 30-mL MB aqueous solution (0.2 mg/mL), which was stirred for 1 h at room temperature. The resultant solid was obtained by centrifugation and washed three times with deionized water. F127 was eliminated by using N,N-dimethylformamide and soaking in ethanol for 48 h at 60°C. Finally, the MB@UiO-66(Ce) product was obtained by vacuum-drying overnight at 60°C.

2.4. MB@UiO-66(Ce) characterization

The morphology of the obtained MB@UiO-66(Ce) was observed by transmission electron microscopy (TEM; FEI Talos L120C, Thermo Scientific, USA). The samples were ultrasonically dispersed in ethanol and dropped on the copper mesh.

The particle size was measured using a particle size analyzer (Nicomp Nano Z3000, PSS, USA). Samples were centrifuged and dispersed in ultrapure water to create 0.5 mg/mL aqueous dispersions, which were sonicated for 5 min before testing.

2.5. Preparation of hydrogel materials

The 50 mM RPS and 1 M SPS aqueous solutions used as stock solutions were applied to initiate the photochemical reactions. Various concentrations of MB@UiO-66(Ce) were mixed in the solution of 1 mL of 30 mg/mL SF and 50 mg/mL gelatin solution with the addition of 20 μL RPS and 10 μL SPS stock solutions, making 0.1%, 0.5%, and 1% w/v the final concentrations of MB@UiO-66(Ce). The hydrogel samples with varying concentrations of MB@UiO-66(Ce) were designated as PH-0, PH-0.1, PH-0.5, and PH-1, respectively. The mixtures were exposed to 460 nm light to initiate photo-crosslinking at an intensity of 1200 mW/cm² for 30 s. The distance used for curing light was 20 mm. The compositions of each group of composites are detailed in Table 1. The 3D-bioprinted MB@UiO-66(Ce)/PH for further cell culture and *in vivo* experiments was fabricated under sterile conditions.

2.6. 3D bioprinting

The BioScaffolder 3.2 (GESIM Corporation, Germany) with extrusion-based 3D-bioprinting technology was used as a low-temperature bioprinting modality. The print head temperature was adjusted to 22.5°C with a speed of 5 mm/s, and the MB@UiO-66(Ce)/PH were printed directly onto the Petri dishes. The hydrogels were printed as hexagons with 7-mm radius and 3-mm height. Finally, the photo-crosslinked hydrogels were formed at a distance of 20 mm using a 3 M Epilar FreeLight 2 LED dental curing lamp with 1200 mW/cm^2 at the source for 30 s.

2.7. Scanning electron microscopy examination

The samples were freeze-dried in a vacuum for 24 h so that the surface microstructures and cross-sectional shapes of the hydrogels could be seen. The samples were then sprayed with gold and examined with a scanning electron microscope (S4800, Japan) at an acceleration voltage of 5 kV.

2.8. Mechanical properties of MB@UiO-66(Ce)/PH

The mechanical properties of the hydrogels were evaluated both via compression tests and tensile tests. In compression tests, hydrogels were prepared using a cylindrical model with height of 10 mm and a diameter of 10 mm. Then, samples were testified at room temperature with speed at 2 mm/min on a universal mechanical tester (HY-0230, China). In tensile tests, hydrogels were prepared using a dumbbell model (dowel: 30 mm in length, 3 mm in width, 2 mm in thickness; bell: 10 mm in length, 15 mm in width, 2 mm in thickness) and stretched using a clamp attachment at a strain rate of 10 mm/min (HY-0230, China).

2.9. Morphological observation of L929 cells on the surface of MB@UiO-66(Ce)/PH

Cells of the 1.5×10^4 mouse fibroblast L929 cell line (CCL-1, ATCC) were cultured on different 3D-bioprinted MB@UiO-66(Ce)/PH for 24 h. Samples were then fixed with 4% polyformaldehyde; cytoskeletons were stained with FITC-phalloidin; and nuclei were stained with DAPI. The morphology of the L929 cells was observed using a confocal laser scanning microscope (CLSM; Leica, Wetzlar, Germany).

2.10. CCK-8 assay

The CCK-8 assay was used to test the viability and proliferation of L929 cells after exposure to the 3D-bioprinted hydrogels. Extracts of 100 μL/well of MB@UiO-66(Ce)/PH were put into 96-well plates, and then 2×10^3 L929 cells were seeded and cultured. Cells were seeded directly in the well plates as a control (CON) group. After cell culture for 1, 3, 5, and 7 days, the CCK-8 working solution was added. The absorbance was measured at 450 nm (Safire, Tecan, Switzerland) after incubation at 37°C for 1.5 h.

2.11. Live/dead assay

The live/dead assay was conducted to evaluate the activity of L929 cells cultured in the MB@UiO-66(Ce)/PH extracts. In this study, the extracts of MB@UiO-66(Ce)/PH were prepared according to the ISO-10993 standard. Then, 1.5×10^4 L929 cells were seeded on glass-bottom culture dishes and cultured for 3 days. DMEM containing 10% FBS was prepared as the CON group. The live/dead staining was implemented according to the manufacturer's instructions. The stained cells were observed using CLSM (Leica, Wetzlar, Germany). Dead cells appeared red whereas living cells appeared green.

2.12. Cell migration assay

The scratch wound healing assay was performed to evaluate the effects of MB@UiO-66(Ce)/PH on cell migration[44]. L929 cells were seeded in 12-well plates, and when the cells reached 90%–100% confluence, a line was scraped in each well using the tip of a sterile plastic pipette and the cells were then treated with MB@UiO-66(Ce)/PH extracts. DMEM containing 10% FBS was prepared as the CON group. All plates were fixed with 4% polyformaldehyde at predetermined time points (0, 6, 12, and 24 h). Finally, they were visualized using a microscope (Ti-U, Nikon, Japan) and calculated using ImageJ software.

2.13. Antibacterial activity of MB@UiO-66(Ce)/PH

Gram-positive *S. aureus* (ATCC 25923) and gram-negative *E. coli* (ATCC 11775) were selected for the detection of antibacterial activity in the MB@UiO-66(Ce)/PH[45]. MB@UiO-66(Ce)/PH were blended with bacteria in a logarithmic phase (10^6 CFU/mL), with or without a 20-min treatment of laser irradiation at 660 nm, 0.5 W/cm^2. The conventional plate counting method was adopted to value the changes in the number of colonies due to the MB@UiO-66(Ce)/PH treatment. The colonies of surviving bacteria after 24 h were calculated using ImageJ software.

2.14. Animal experiments

All animal experiments in this study were conducted in accordance with the guidelines for the protection of animal life and protocols approved by the Institutional Animal Care and Use Committee (SH9H-2021-A32-1) and following the Animal Experimental Ethical Inspection procedure of the Ninth People's Hospital, which is affiliated with the Shanghai Jiao Tong University School of Medicine.

A full-thickness skin defect mouse model was adopted to investigate the effects of MB@UiO-66(Ce)/PH treatment on skin wound repair *in vivo*. Briefly, the full-thickness defect model was established using 8-week-old Kunming mice. Wounds were made using a sterile, 5-mm biopsy punch outlining two circular wound patterns on each side of the mouse midline. The skin in the middle of the outline was lifted with serrated forceps; a full-thickness wound was created with iris scissors that extend into the subcutaneous tissue; and this circular tissue was excised. *S. aureus* (50 μL, 1×10^6 CFU/mL) was injected at the wound sites on the next day to simulate infection. Day 0 was designated as the first day of infection. All mice were randomly divided into five groups (PH-0, PH-0.1, PH-0.5, PH-1, and CON group), and mice in different groups received implantation at the wound sites with a different dose of MB@UiO-66(Ce)/PH on day 1. All hydrogel dressings were circular in shape, with a diameter of 5 mm and a height of 0.5 mm. Mice that were treated with only sterilized phosphate-buffered saline were used as the CON group.

Following surgery, mice were photographed at predetermined time points (1, 3, 7, 10, and 14 days) and sacrificed at either 7 or 14 days. The wound areas were estimated using ImageJ software. The tissues at the infected sites were dissected and fixed in a 4% formaldehyde solution for 24 h. Next, the tissues were embedded in molten paraffin for staining[46]. Sections were stained with hematoxylin and eosin (H&E) for H&E staining and hematoxylin, acid fuchsin solution, and aniline blue for Masson's trichrome staining.

2.15. Statistical analysis

All data were presented as the mean ± standard deviation. One-way analysis of variance (ANOVA) and *t*-test analyses were used to analyze the data for all groups. A $p < 0.05$ was considered statistically significant.

3. Results and discussion

3.1. Preparation and characterization of MB@UiO-66(Ce)

TEM images show MB@UiO-66(Ce) crystals with particle sizes of ≈110 nm were successfully obtained. **Figure S1** shows that large, open mesopores were periodically distributed throughout UiO-66(Ce), and MB was successfully loaded on the NPs. TEM images further confirmed that the NPs were well-dispersed, and the ordered large mesopores were uniformly distributed across the entire sample. The NP sizes were further examined by dynamic laser scattering. Similar to the TEM observations, the MB@UiO-66(Ce) particle size was mainly distributed around 110.22 ± 11.85 nm, as shown in **Figure S2**.

3.2. Preparation and characterization of MB@UiO-66(Ce)/PH dressing

Photo-crosslinked hydrogel systems used for 3D-bioprinting were obtained by mixing gelatin into SF and using riboflavin and SPS as crosslinking agents. Figure 2A shows the 3D-bioprinted dressings in a hexagonal grid pattern. MB@UiO-66(Ce) was added to the hydrogels in different proportions, and hydrogel dressings were constructed via bioprinting as hexagonal scaffolds with the dimensions of 7-mm radius, 2-mm height, and 1-mm grid. Figure 2B shows that the MB@UiO-66(Ce)/PH dressing had a rough surface for cell adhesion and a 1-mm grid formed by 3D bioprinting, which is consistent with the designed grid pattern (**Figure S3**). Meanwhile, the TEM image shows that MB@UiO-66(Ce)/PH dressings were spongy with porous interiors in the cross-section. Figure 2C shows the compressive strain–stress curve of MB@UiO-66(Ce)/PH, the compressive strength of PH-1 hydrogel is ~45 kPa, while the compressive strength of the composite hydrogel significantly increased with the increase of NPs concentration (Figure 2D). Comparing the above hydrogels, Figure 2E and F shows that PH-1 hydrogel possessed a relatively higher elongation (51%) and a higher tensile strength (2.6 kPa) compared with other groups. In summary, the tensile stress of the hydrogels increased with the amount of the incorporated NPs.

3.3. Effect of hydrogels on activity and proliferation of L929 cells

Early cell adhesion is an important factor in subsequent biological behavior[47]. The cytoskeletons of L929 cells were stained and observed after being cultured with different MB@UiO-66(Ce)/PH levels for 12 h. As shown in Figure 3A, L929 cells adhered and spread well with polygonal structures on the surface of the hydrogels.

The cells in the five groups significantly increased with time. Figure 3B shows that the hydrogel groups proliferated slightly faster than the nonimplant group (CON) in the early stage, but there was no significant difference at 7 days. This may be related to the porous structure of hydrogel, which facilitates cell proliferation. At the same time, the hydrogel coating slows the UiO-66(Ce) release and thus reduces the toxicity of NPs. It is also shown that UiO-66(Ce) loaded with MB can effectively reduce the photosensitizer cytotoxicity in nearby cells. These results suggest that the hydrogel has good biocompatibility and no effect on the adhesion and proliferation of L929 cells.

3.4. Cytotoxicity of the hydrogels were detected by the CCK-8 test

L929 cells were incubated in the extracts for 3 days and stained with the live/dead kit. Live cells were stained with calcein AM (green fluorescence), whereas dead cells were stained with propidium iodide (red fluorescence). The live/dead assay showed that almost no red fluorescence spots appeared in the whole group (Figure 3C). The comparatively high cellular activity within the extracts indicated good biocompatibility of the gel materials.

3.5. Cell migration

Cell migration is essential for promoting wound healing[48]. To explore whether the hydrogels affected the migration of cells, we performed cell migration experiments. In different groups, L929 cells migrated from the surrounding region to the cell-free region after a 24-h culture. Figure 4A shows that cells in all groups gradually migrated to the scratched area. In the early stage, the cell migration rate was the

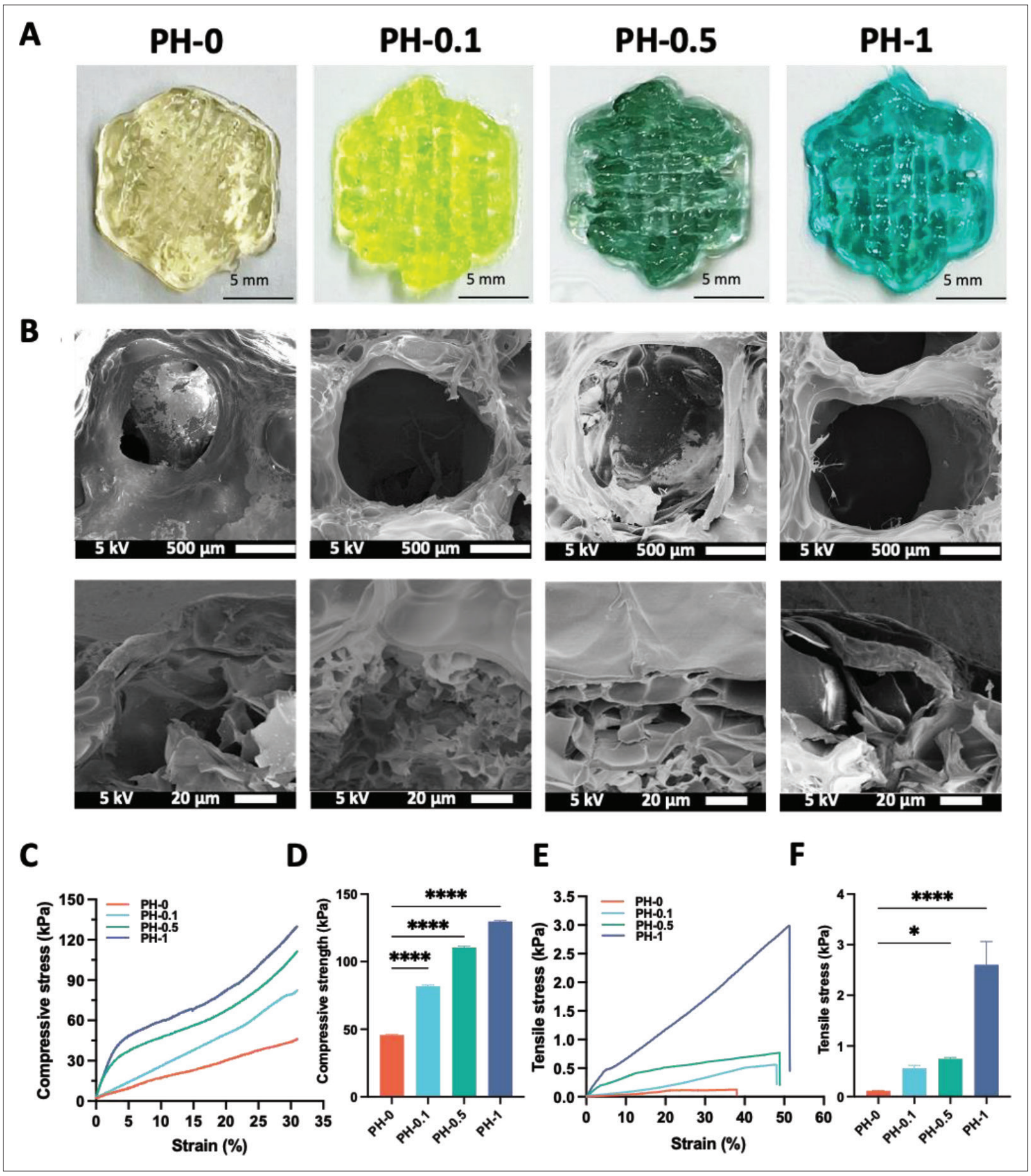

Figure 2. Construction and characterization of MB@UiO-66(Ce)-SF/gelatin nanocomposite 3D-bioprinted hydrogel. (A) Photographs of 3D bioprinted PH-0, PH-0.1, PH-0.5, and PH-1 hydrogels. Scale bar: 5 mm. (B) SEM images of PH-0, PH-0.1, PH-0.5, and PH-1 hydrogels. Scale bar: 500 and 20 µm. (C) Compression stress strain curves of PH-0, PH-0.1, PH-0.5, and PH-1 hydrogels. (D) Compression strength of PH-0, PH-0.1, PH-0.5, and PH-1 hydrogels. (E) Tensile stress–strain curves of PH-0, PH-0.1, PH-0.5, and PH-1 hydrogels. (F) Tensile strength of PH-0, PH-0.1, PH-0.5, and PH-1 hydrogels. Data are means ± SD; *n* = 3. $^{*}p < 0.05$, $^{****}p < 0.0001$.

fastest in the MB@UiO-66(Ce)/PH groups compared with the CON group, as shown in Figure 4B. These results suggest that cells in the hydrogels have better migration ability than cells in the CON group.

3.6. Antibacterial ability of hydrogels

We quantified the antibacterial activity of the hydrogels against clinically common bacteria by using the plate count method. Colony counts decreased in the 660 nm laser irradiation + hydrogel group compared to the CON group, while the hydrogel alone group showed no bactericidal effect. Figure 5A and B shows that the PH-0 hydrogel had no effect on bacteria, with or without light (660 nm). Furthermore, MB@UiO-66(Ce) did not kill any bacteria in the absence of light. On the contrary, after 20 min of light exposure, MB@UiO-66(Ce) reduced the viability of *S. aureus* and *E. coli* compared to the CON group. The antibacterial effect became more pronounced as the concentration increased. In the PH-1 group, most bacteria died after light exposure, as shown in Figure 5C and D.

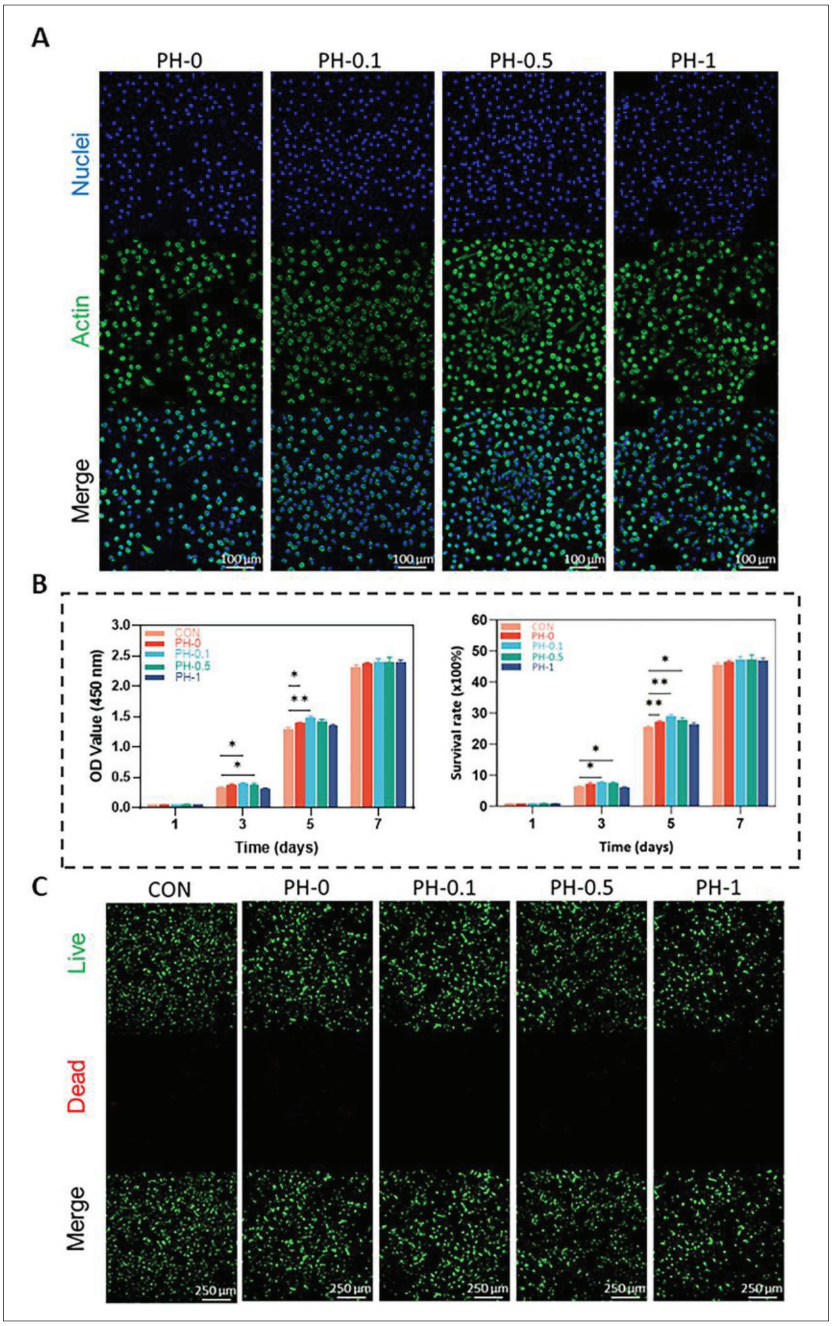

Figure 3. Influence of 3D bioprinted MB@UiO-66(Ce)/PH on the behavior of L929 cells *in vitro*. (A) The adhesion of L929 cells cultured on the PH-0, PH-0.1, PH-0.5, and PH-1 hydrogels after 12 h. Scale bar: 100 µm. (B) Quantitative analysis of the proliferation of L929 cells cultured with hydrogels by CCK-8. Data are means ± SD; $n = 3$. *$p < 0.05$, **$p < 0.01$. (C) *In vitro* live/dead assay of L929 cells cultured on MB@UiO-66(Ce)/PH, live cells (green), and dead cells (red). Scale bar: 250 µm.

These results verified the photodynamic antibacterial properties of MB@UiO-66(Ce). It is worth noting that the NPs contain low amounts of MB, as mentioned above. This good photodynamic antimicrobial activity also highlights the fact that utilizing UiO-66(Ce) loaded with MB allows for a more uniform dispersion, which facilitates the production of $^1O_2$ under light.

3.7. *In vivo* wound healing in a full-thickness skin defect model

An infected full-thickness skin defect mouse model was adopted to evaluate the *in vivo* wound healing performance of MB@UiO-66(Ce)/PH as a potential wound dressing Figure 6A. As shown in Figure 6B, the wound areas in all five groups healed with time. At any

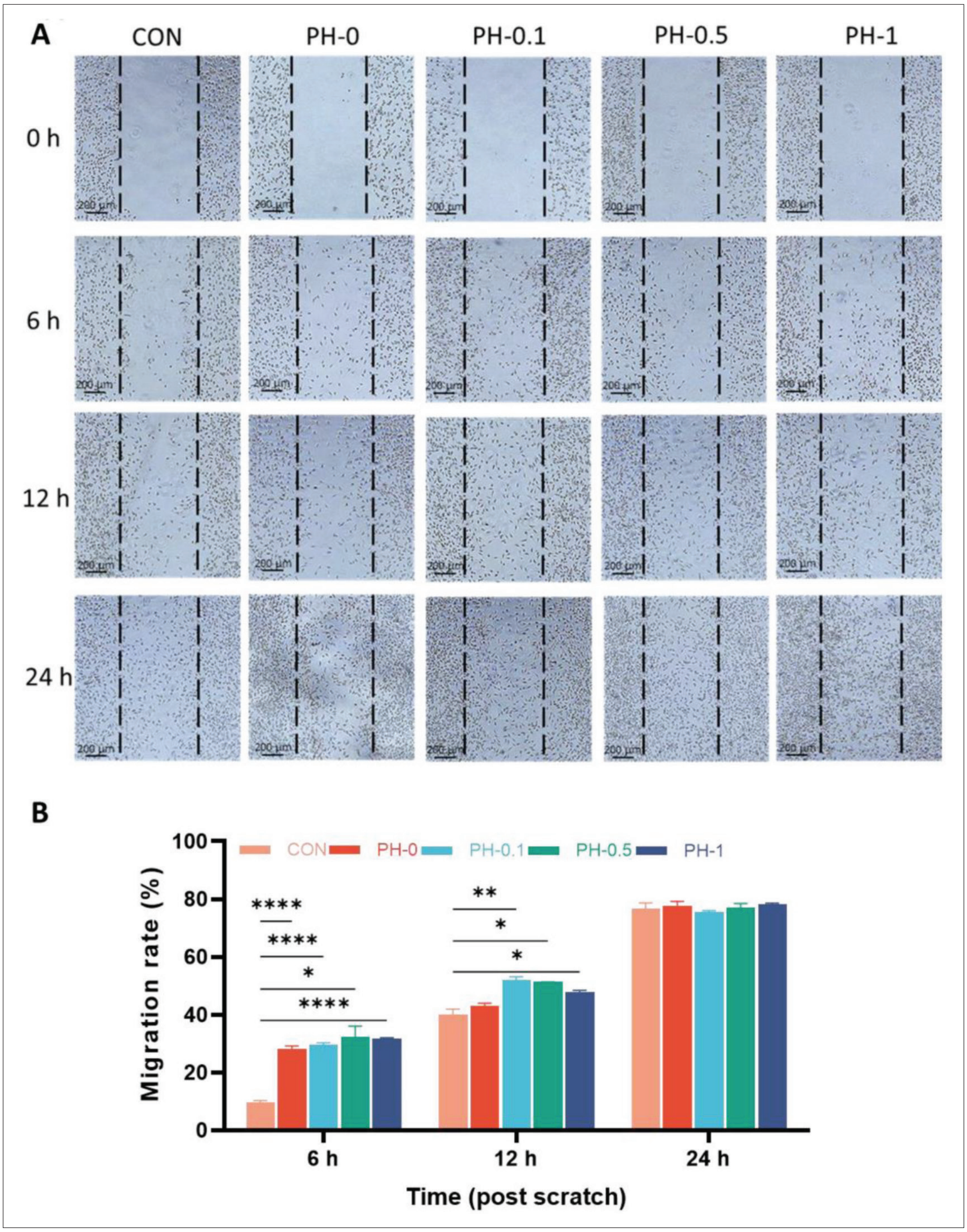

Figure 4. The migration of L929 cells under conditioned extraction of hydrogels in the wound healing assay. (A) Photographs of L929 cells at 0, 6, 12, and 24 h after wound healing. (B) The quantification of migrating fibroblasts. Data are means ± SD; *n* = 3. $^{*}p < 0.05$, $^{**}p < 0.01$, $^{****}p < 0.0001$.

point after the operation, the wound areas in the hydrogel groups were much smaller than those in the CON group. The simulation diagram (Figure 6C) and data statistics (Figure 6D) show the same trend. Meanwhile, the hydrogels showed better healing results compared to the CON group and could significantly reduce the wound healing time. In addition, Figure 6C and D shows that even without NPs, PH-0 is advantageous for wound healing. Furthermore, the rate of wound healing, which is significantly affected by bacterial infection, was significantly increased as the antimicrobial properties of the material improved, indicating that the antimicrobial

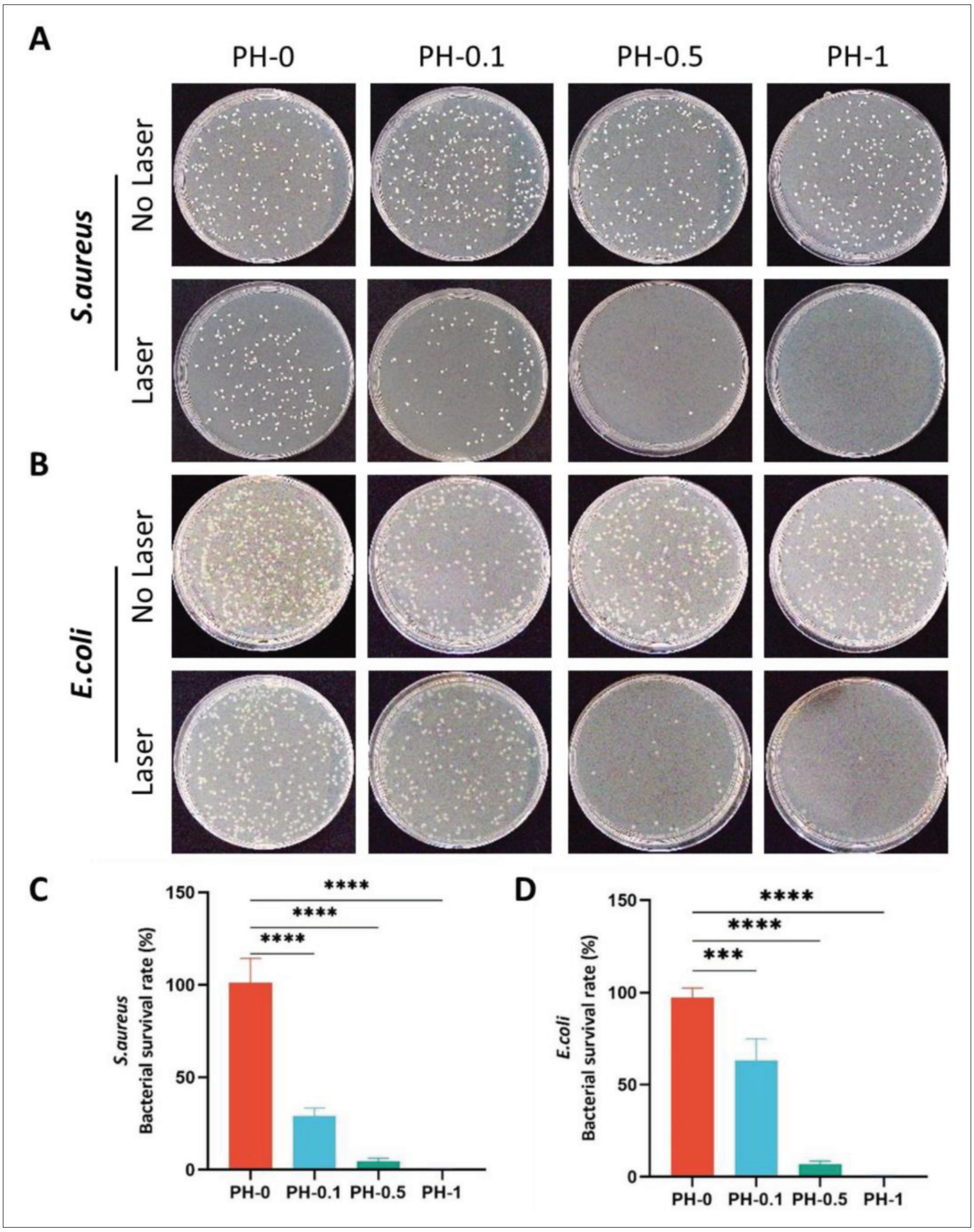

Figure 5. Photodynamics regulation of bacterial behavior *in vitro* under 660-nm light. Plate colony count images of (A) *S. aureus* and (B) *E. coli* co-cultured with hydrogels under 660-nm light. (C, D) The corresponding antibacterial ratio statistics. Data are means ± SD; $n = 4$. $****p < 0.0001$.

dressings were particularly effective in promoting infected wound healing.

3.8. Histological evaluation of regenerated tissues

The paraffin sections were prepared and observed by H&E staining and Masson's trichrome staining to evaluate the effect of MB@UiO-66(Ce)/PH on skin defect healing *in vivo*. The H&E staining results showed that 7 days after the operation, a large number of inflammatory cells could be seen around the wound site in the CON and non-nanoparticle hydrogel (PH-0) groups, as shown in Figure 7A. In contrast, there was no obvious inflammatory cell infiltration in the three hydrogel implantation groups containing NPs. In addition, in the PH-0.1, PH-0.5, and PH-1 groups containing NPs, partial epithelial crawling repair was observed on the surface. Compared with the

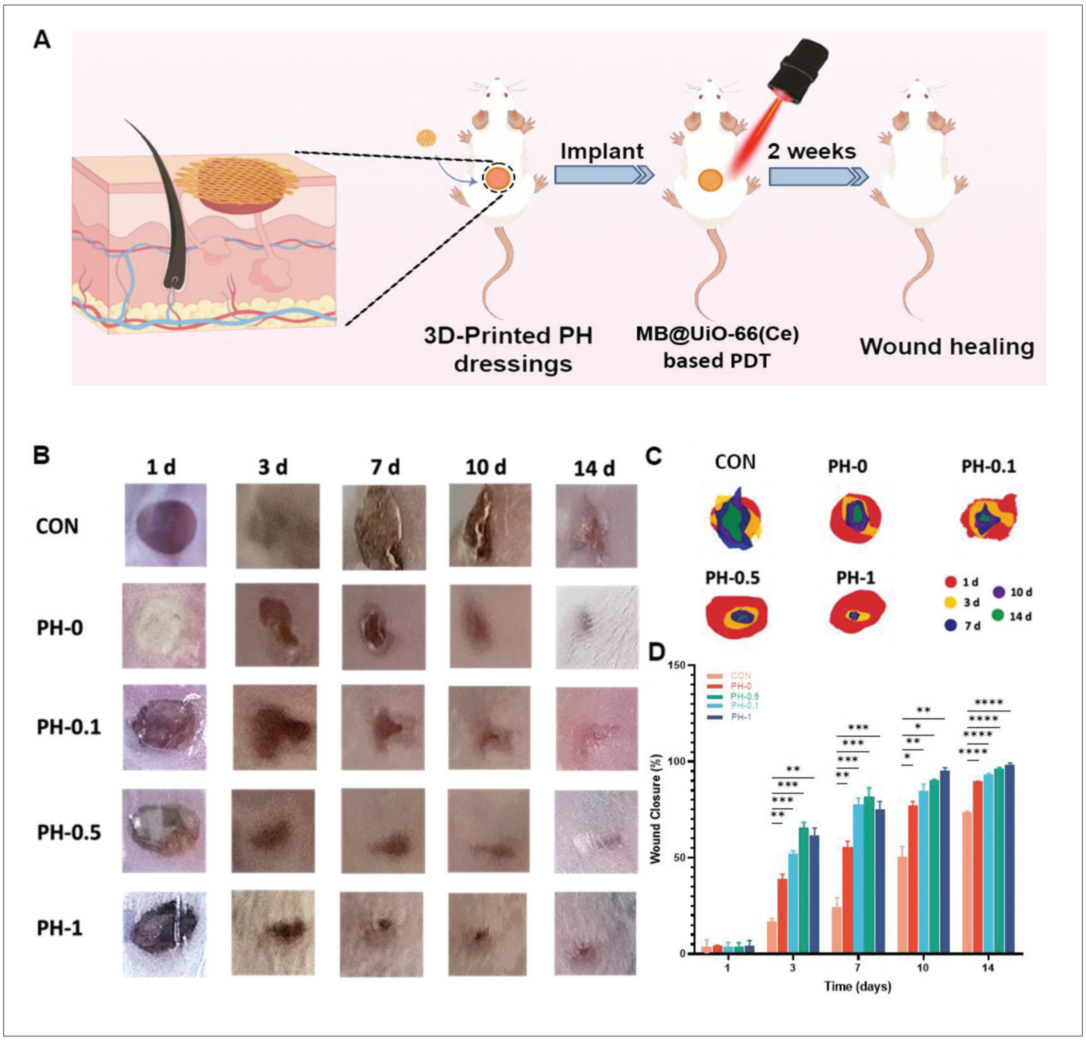

Figure 6. Photodynamics regulation of infected wound repair *in vivo* under 660 nm light. (A) The strategy of photodynamics therapy *in vivo*. (B) Representative images of the incisional skin wounds treated with hydrogels at determined time and (C) the corresponding simulation of wound area. (D) Quantitative analysis of the wound area evolution rate of different groups. Data are means ± SD; $n = 3$. $^{*}p < 0.05$, $^{**}p < 0.01$, $^{***}p < 0.001$, $^{****}p < 0.0001$.

CON group, more fibroblasts and thicker granulation tissue were observed around the damaged area in these three groups, indicating that MB@UiO-66(Ce)/PH has good biocompatibility and does not cause a serious immune reaction during the early stage of wound infection, which is related to the low immunogenicity of SF and the cell-like structure of gelatin in the 3D bioprinting of hydrogel matrix.

Figure 7A shows the healing process at 7 and 14 days of different groups. H&E staining 14 days after surgery revealed that the defect area of the CON group failed to form a good epithelial barrier. Despite the basic structure of the epithelium and dermis, tissue regeneration was not completely formed during the repair process, and there was a slight inflammatory reaction. In the implanted MB@UiO-66(Ce)/PH group, complete epithelial crawling was observed in the defect area, and there was no obvious inflammatory cell infiltration. Compared to the CON group, the epidermis and epithelial structures that developed in the PH-0.5 and PH-1 groups were more complete and uniform; fibroblasts were placed more systematically; and the dermis had new blood vessels and hair follicles. These indicated that MB@UiO-66(Ce)/PH containing NPs has a good wound healing effect and can prevent the bacterial invasion, thus promoting wound healing.

The formation and orderly arrangement of collagen are important in the process of skin tissue repair and remodeling and also have an important impact on the tensile strength of granulation tissue[49]. As shown in Figure 7B, all groups showed collagen deposition on the 7 and 14 days after operation. Compared with other groups, wounds in the CON group showed less collagen deposition,

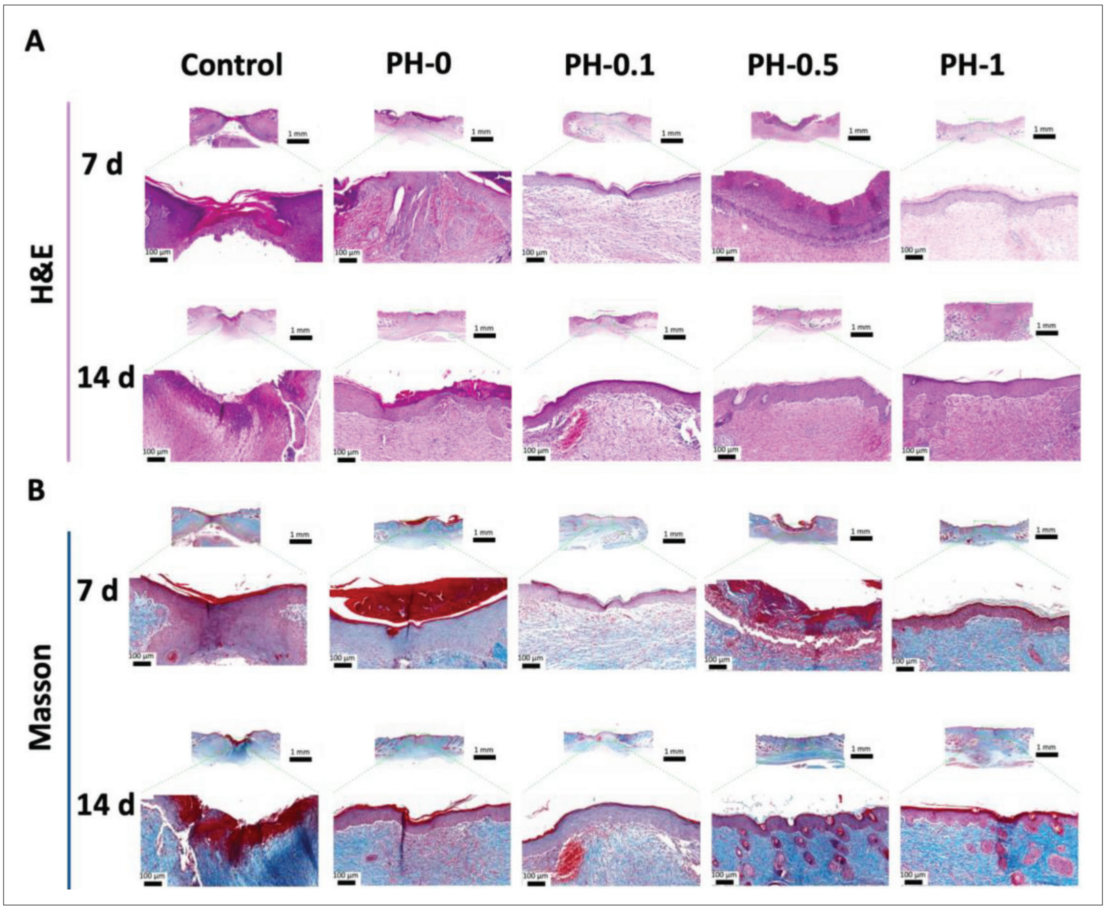

Figure 7. Photodynamics regulation of infected wound repair *in vivo* under 660 nm light. (A) H&E staining and (B) Masson's trichrome staining of the wound tissue in different groups for pathological evaluation after treatment.

whereas wounds treated with hydrogel showed higher collagen density and fibrous structure at all time points. Compared with other groups, hydrogel groups containing more NPs (PH-0.5 and PH-1) showed obvious collagen deposition, neovascularization in the dermis, and some skin appendages on the 14 days. These results indicated that MB@UiO-66(Ce)/PH-containing NPs greatly enhance collagen deposition during wound healing.

In this study, the infected wound model was used. On the 7th day after the defect operation, only part of the epidermis in the blank group crawled and connected. On the 14th day of wound repair, the group without implanted materials could not achieve complete wound repair, and wound healing was blocked. Groups with MB@UiO-66(Ce)/PH dressing, even without NPs, showed better repair than the CON group. This may be related to the material occupying the defect area, which is conducive to the crawling of fibroblasts and subsequent promotion of epithelial formation[50]. When more NPs were added, skin formation was improved due to the antibacterial effect of the NPs. Due to the wound formation, the skin tissue is more vulnerable to bacterial invasion, especially in the presence of chronic diseases such as diabetes, and infection is more likely to occur, which will hinder the repair and regeneration of skin tissue. Therefore, after wound formation, antibacterial therapy is particularly important for follow-up repair of the tissue[51]. In this study, the hydrogel group containing more NPs (PH-0.5 and PH-1) had good biocompatibility, no obvious inflammatory reaction after 7 days of implantation, and earlier epithelial coverage. On the 14th day, there were good skin appendages in the dermis, indicating a good skin healing effect. In summary, the prepared PH gel was conducive to epithelium formation, collagen deposition, and repair of appendages in infected wounds under the action of composite antibacterial NPs and can promote the healing of infected wounds.

4. Conclusion

In this study, we developed a composite photo-crosslinked SF/gelatin hydrogel loaded with MB@UiO-66(Ce) NPs and further 3D bioprinted it with customized structures for wound dressings. We also characterized the printability of MB@UiO-66(Ce)/PH hydrogel and improved the mechanical properties of the hydrogel using nanoparticles. At the same time, the hydrogels were shown to have good biocompatibility and to promote early cell adhesion and migration. This 3D-bioprinted dressing also has antibacterial properties from the PDT effect of MB@UiO-66(Ce) NPs and promotes the healing of infected wounds. With a 20-min laser irradiation treatment, the MB@UiO-66(Ce)/PH significantly reduced the viability of *S. aureus* and *E. coli*. The antibacterial capacity of the hydrogels increased with the concentration of NPs. Meanwhile, after a 7-day treatment with PH-1, the full-thickness skin defects in mice were repaired, and the hydrogels showed better healing effects. In conclusion, the prepared 3D-bioprinted composite photo-crosslinked MB@UiO-66(Ce)/PH with good antibacterial properties and tissue healing-promoting ability provides a new strategy involving 3D bioprinting for preparing wound dressings.

Acknowledgments

None.

Funding

This research was funded by the National Natural Science Foundation of China (Nos. 82100963, 82270953 and 81971840), Shanghai Rising-Star Program (21QA1405400), and Natural Science Foundation of Shanghai (22ZR1436400).

Conflict of interest

The authors declare they have no competing interests.

Author contributions

Conceptualization: Wei Wang, Yang Liu, Chen Wang
Formal analysis: Zhuoyuan Li, Ao Zheng, Zhiyuan Mao
Investigation: Zhuoyuan Li, Ao Zheng
Methodology: Zhuoyuan Li, Ao Zheng, Fupeng Li, Tingshu Su
Writing – original draft: Zhuoyuan Li, Ao Zheng, Lingyan Cao, Tingshu Su
Writing – review & editing: Wei Wang, Yang Liu, Chen Wang

Ethics approval and consent to participate

All experimental protocols in the study were conducted according to the guidelines of the Declaration of Helsinki and approved by the Institutional Ethics Committee of Shanghai Ninth People's Hospital, Shanghai Jiao Tong University School of Medicine (SH9H-2021-A32-1). All methods were carried out in accordance with relevant guidelines and regulations.

Consent for publication

Not applicable.

Availability of data

The data underlying this article will be shared on reasonable request to the corresponding author.

References

1. Kechichian E, Ezzedine K, 2018, Vitamin D and the skin: An update for dermatologists. *Am J Clin Dermatol*, 19: 223–235.
2. Falcone M, De Angelis B, Pea F, *et al.*, 2021, Challenges in the management of chronic wound infections. *J Global Antimicrob Resist*, 26: 140–147.
3. Kathawala MH, Ng WL, Liu D, *et al.*, 2019, Healing of chronic wounds: An update of recent developments and future possibilities. *Tissue Eng Part B Rev*, 25: 429–444.
4. Simoes D, Miguel SP, Ribeiro MP, *et al.*, 2018, Recent advances on antimicrobial wound dressing: A review. *Eur J Pharm Biopharm*, 127: 130–141.
5. Yang N, Zhu M, Xu G, *et al.*, 2020, A near-infrared light-responsive multifunctional nanocomposite hydrogel for efficient and synergistic antibacterial wound therapy and healing promotion. *J Mater Chem B*, 8: 3908–3917.
6. White RJ, Cutting K, Kingsley A, 2006, Topical antimicrobials in the control of wound bioburden. *Ostomy/Wound Manage*, 52: 26–58.
7. Zhao G, Hochwalt PC, Usui ML, *et al.*, 2010, Delayed wound healing in diabetic (db/db) mice with *Pseudomonas aeruginosa* biofilm challenge: A model for the study of chronic wounds. *Wound Repair Regen*, 18: 467–477.
8. Li S, Dong S, Xu W, *et al.*, 2018, Antibacterial hydrogels. *Adv Sci*, 5: 1700527.
9. Dai X, Zhao Y, Yu Y, *et al.*, 2017, Single continuous near-infrared laser-triggered photodynamic and photothermal ablation of antibiotic-resistant bacteria using effective targeted copper sulfide nanoclusters. *ACS Appl Mater Interfaces*, 9: 30470–30479.
10. Van Vlierberghe S, Dubruel P, Schacht E, 2011, Biopolymer-based hydrogels as scaffolds for tissue engineering applications: A review. *Biomacromolecules*, 12: 1387–1408.
11. Bilici C, Can V, Nöchel U, *et al.*, 2016, Melt-processable shape-memory hydrogels with self-healing ability of high mechanical strength. *Macromolecules*, 49: 7442–7449.
12. Tavakoli S, Klar AS, 2020, Advanced hydrogels as wound dressings. *Biomolecules*, 10: 1169.
13. Koehler J, Brandl FP, Goepferich AM, 2018, Hydrogel wound dressings for bioactive treatment of acute and chronic wounds. *Eur Polym J*, 100: 1–11.

14. Gupta P, Vermani K, Garg S, 2002, Hydrogels: From controlled release to pH-responsive drug delivery. *Drug Discov Today*, 7: 569–579.
15. Augustine R, 2018, Skin bioprinting: A novel approach for creating artificial skin from synthetic and natural building blocks. *Prog Biomater*, 7: 77–92.
16. Ng WL, Huang X, Shkolnikov V, *et al.*, 2022, Controlling droplet impact velocity and droplet volume: Key factors to achieving high cell viability in sub-nanoliter droplet-based bioprinting. *Int J Bioprint*, 8: 17, 424.
17. Ng WL, Lee JM, Zhou MM, *et al.*, 2020, Vat polymerization-based bioprinting-process, materials, applications and regulatory challenges. *Biofabrication*, 12: 22, 022001.
18. Jiang T, Munguia-Lopez JG, Flores-Torres S, *et al.*, 2019, Extrusion bioprinting of soft materials: An emerging technique for biological model fabrication. *Appl Phys Rev*, 6: 30, 011310.
19. Chocarro-Wrona C, de Vicente J, Antich C, *et al.*, 2021, Validation of the 1, 4-butanediol thermoplastic polyurethane as a novel material for 3D bioprinting applications. *Bioeng Transl Med*, 6: e10192.
20. Vijayavenkataraman S, Lu W, Fuh J, 2016, 3D bioprinting of skin: A state-of-the-art review on modelling, materials, and processes. *Biofabrication*, 8: 032001.
21. Mandrycky C, Wang Z, Kim K, *et al.*, 2016, 3D bioprinting for engineering complex tissues. *Biotechnol Adv*, 34: 422–434.
22. Axpe E, Oyen ML, 2016, Applications of alginate-based bioinks in 3D bioprinting. *Int J Mol Sci*, 17: 1976.
23. Shao Z, Vollrath F, 2002, Surprising strength of silkworm silk. *Nature*, 418: 741–741.
24. Müller M, Becher J, Schnabelrauch M, *et al.*, 2015, Nanostructured pluronic hydrogels as bioinks for 3D bioprinting. *Biofabrication*, 7: 035006.
25. Wang Z, Abdulla R, Parker B, *et al.*, 2015, A simple and high-resolution stereolithography-based 3D bioprinting system using visible light crosslinkable bioinks. *Biofabrication*, 7: 045009.
26. Melke J, Midha S, Ghosh S, *et al.*, 2016, Silk fibroin as biomaterial for bone tissue engineering. *Acta Biomater*, 31: 1–16.
27. Kim SH, Kim DY, Lim TH, *et al.*, 2020, Silk fibroin bioinks for digital light processing (DLP) 3D bioprinting. *Bioinspired Biomater Adv Tissue Eng Regen Med*, 1249: 53–66.
28. Kambe Y, Mizoguchi Y, Kuwahara K, *et al.*, 2020, Beta-sheet content significantly correlates with the biodegradation time of silk fibroin hydrogels showing a wide range of compressive modulus. *Polym Degrad Stab*, 179: 109240.
29. Zheng A, Wang X, Xin X, *et al.*, 2023, Promoting lacunar bone regeneration with an injectable hydrogel adaptive to the microenvironment. *Bioact Mater*, 21: 403–421.
30. Piluso S, Gomez DF, Dokter I, *et al.*, 2020, Rapid and cytocompatible cell-laden silk hydrogel formation via riboflavin-mediated crosslinking. *J Mater Chem B*, 8: 9566–9575.
31. Lee H, Shin D, Shin S, *et al.*, 2020, Effect of gelatin on dimensional stability of silk fibroin hydrogel structures fabricated by digital light processing 3D printing. *J Ind Eng Chem*, 89: 119–127.
32. Billiet T, Gevaert E, De Schryver T, *et al.*, 2014, The 3D printing of gelatin methacrylamide cell-laden tissue-engineered constructs with high cell viability. *Biomaterials*, 35: 49–62.
33. Planas O, Bresolí-Obach R, Nos J, *et al.*, 2015, Synthesis, photophysical characterization, and photoinduced antibacterial activity of methylene blue-loaded amino- and mannose-targeted mesoporous silica nanoparticles. *Molecules*, 20: 6284–6298.
34. Lucky SS, Soo KC, Zhang Y, 2015, Nanoparticles in photodynamic therapy. *Chem Rev*, 115: 1990–2042.
35. Chen QW, Liu XH, Fan JX, *et al.*, 2020, Self-mineralized photothermal bacteria hybridizing with mitochondria-targeted metal–organic frameworks for augmenting photothermal tumor therapy. *Adv Funct Mater*, 30: 1909806.
36. Tummers QR, Boonstra MC, Frangioni JV, *et al.*, 2015, Intraoperative near-infrared fluorescence imaging of a paraganglioma using methylene blue: A case report. *Int J Surg Case Rep*, 6: 150–153.
37. Wang Z, Hu S, Yang J, *et al.*, 2018, Nanoscale zr-based MOFs with tailorable size and introduced mesopore for protein delivery. *Adv Funct Mater*, 28: 1707356.
38. Dhakshinamoorthy A, Navalón S, Asiri AM, *et al.*, 2020, Gold-nanoparticle-decorated metal-organic frameworks for anticancer therapy. *ChemMedChem*, 15: 2236–2256.
39. Gupta V, Mohiyuddin S, Sachdev A, *et al.*, 2019, PEG functionalized zirconium dicarboxylate MOFs for docetaxel drug delivery in vitro. *J Drug Deliv Sci Technol*, 52: 846–855.
40. Kaur N, Tiwari P, Kapoor KS, *et al.*, 2020, Metal–organic framework based antibiotic release and antimicrobial response: An overview. *CrystEngComm*, 22: 7513–7527.
41. Liu Y, Zhou L, Dong Y, *et al.*, 2021, Recent developments on MOF-based platforms for antibacterial therapy. *RSC Med Chem*, 12: 915–928.
42. Lázaro IA, Forgan RS, 2019, Application of zirconium MOFs in drug delivery and biomedicine. *Coord Chem Rev*, 380: 230–259.
43. Ding Q, Xu Z, Zhou L, *et al.*, 2022, A multimodal metal-organic framework based on unsaturated metal site for enhancing antitumor cytotoxicity through chemo-photodynamic therapy. *J Colloid Interface Sci*, 621: 180–194.
44. Zhang XY, Kang XN, Jin LJ, *et al.*, 2018, Stimulation of wound healing using bioinspired hydrogels with basic

fibroblast growth factor (bFGF). *Int J Nanomed*, 13: 3897–3906.

45. Huang K, Li FP, Yuan K, *et al.*, 2022, A MOF-armored zinc-peroxide nanotheranostic platform for eradicating drug resistant bacteria via image-guided and in situ activated photodynamic therapy. *Appl Mater Today*, 28: 12, 101513.

46. Xu ZQ, Qi XY, Bao MY, *et al.*, 2023, Biomineralization inspired 3D printed bioactive glass nanocomposite scaffolds orchestrate diabetic bone regeneration by remodeling micromilieu. *Bioact Mater*, 25: 239–255.

47. Yoshinari M, Hayakawa T, Matsuzaka K, *et al.*, 2006, Oxygen plasma surface modification enhances immobilization of simvastatin acid. *Biomed Res*, 27: 29–36.

48. Sun X, Song W, Teng L, *et al.*, 2023, MiRNA 24-3p-rich exosomes functionalized DEGMA-modified hyaluronic acid hydrogels for corneal epithelial healing. *Bioact Mater*, 25: 640–656.

49. Zhang Z, Li W, Liu Y, *et al.*, 2021, Design of a biofluid-absorbing bioactive sandwich-structured Zn–Si bioceramic composite wound dressing for hair follicle regeneration and skin burn wound healing. *Bioact Mater*, 6: 1910–1920.

50. Liang Y, He J, Guo B, 2021, Functional hydrogels as wound dressing to enhance wound healing. *ACS Nano*, 15: 12687–12722.

51. Liang Y, Liang Y, Zhang H, *et al.*, 2022, Antibacterial biomaterials for skin wound dressing. *Asian J Pharm Sci*, 17: 353–384.